Complex magnetic phases enriched by charge density waves in the topological semimetals $GdSb_xTe_{2-x-\delta}$

Shiming Lei,[1] Audrey Saltzman,[2] and Leslie M. Schoop[1,*]
[1]*Department of Chemistry, Princeton University, Princeton, New Jersey 08544, USA*
[2]*Department of Physics, Massachusetts Institute of Technology, Cambridge, Massachusetts 02139, USA*

(Received 25 November 2020; accepted 31 March 2021; published 13 April 2021)

The interplay of crystal symmetry, magnetism, band topology, and electronic correlation can be the origin of quantum phase transitions in condensed matter. Particularly, square-lattice materials have been serving as a versatile platform to study the rich phenomena resulting from that interplay. In this work we report a detailed magnetic study on the square-lattice-based magnetic topological semimetal $GdSb_xTe_{2-x-\delta}$. We report the *H-T* magnetic phase diagrams along three crystallographic orientations and show that, for those materials where a charge density wave distortion is known to exist, many different magnetic phases are identified. In addition, the data hints towards the existence of an antiferromagnetic skyrmion phase, which has been theoretically predicted but not experimentally confirmed in a bulk material yet.

DOI: 10.1103/PhysRevB.103.134418

I. INTRODUCTION

Square-net materials that exhibit a delocalized, hypervalent chemical bond have been established to be a versatile material platform to host topological electronic states [1]. One interesting class of square-net compounds is the *MXZ* family that crystallizes in the PbFCl-structure, with space group $P4/nmm$. An example is the topological nodal-line semimetal ZrSiS. Its crystal structure highlights a square net of Si atoms that are separated by a puckered ZiS bilayer [2]. The band structure near the Fermi level (E_F) features linear band-crossings which mostly result from the Si p_x and p_y bands. Without spin-orbit coupling (SOC), these linear band crossing points (Dirac nodes) connect to form a diamond-shaped loop.

In addition to such nonmagnetic topological materials, magnetic analogs can be also found in the *MXZ* family [3]. Particularly, *Ln*SbTe materials (*Ln* = lanthanide) that are isostructural and isoelectronic to ZrSiS have been explored as promising candidates [4–11]. The introduction of magnetic order can significantly enrich the physics of *MXZ* compounds. For example, it provides an opportunity to access new topological electronic states by breaking time-reversal symmetry; furthermore, the control of magnetic order provides an additional knob to tune the electronic structure and drive it through a manifold of topologically distinct phases [4]. Such interplay of band topology and magnetism would be especially appealing for spintronic applications, such as topological antiferromagnetic spintronics [12].

Beyond the aforementioned properties, *Ln*SbTe materials also provide a platform to study the physics of charge density waves (CDWs) when the compounds are off-stoichiometric. In the nonmagnetic $LaSb_xTe_{2-x}$, DiMasi *et al.* have reported that the CDW wave vector can be continuously tuned along with the Sb composition, x, from 0 to 1, which is in accordance with the picture of continuous change of band filling and Fermi surface nesting [13]. As an extension, we recently explored the antiferromagnetic $GdSb_xTe_{2-x-\delta}$ series (δ indicates the vacancy level) and found that this system can be tuned to have either commensurate or incommensurate lattice modulations, depending on the Sb content. Compared to $LaSb_xTe_{2-x}$, where a CDW appears when $x < 1$, in $GdSb_xTe_{2-x-\delta}$ the nondistorted tetragonal phase is stable for $0.85 < x < 1$ [9].

Based on the observation of CDWs and band crossings protected by nonsymmorphic symmetry [2,14], we suggested a strategy for using the CDW as a tool to create idealized nonsymmorphic Dirac semimetals in the *Ln*SbTe phases [15]. We showed that the electronic structure of $GdSb_{0.46}Te_{1.48}$ near E_F features clean nonsymmorphic nodal-line Dirac states, while other states at E_F are suppressed by CDWs. Since the magnetic susceptibility is affected by the Fermi energy in nodal-line semimetals [16,17], it would be of particular interest to understand the evolution of the magnetism with varying band filling (in this case, varying Sb content) in the $GdSb_xTe_{2-x-\delta}$ system.

Here we report a systematic study of the magnetic properties of $GdSb_xTe_{2-x-\delta}$, with a focus on the compounds with CDW distortions ($x < 0.85$), where we especially highlight the nodal-line semimetal $GdSb_{0.46}Te_{1.48}$. By magnetic susceptibility decoupling and mechanical detwinning, we are able to establish *H-T* magnetic phase diagrams along all three crystallographic orientations for $GdSb_{0.46}Te_{1.48}$. The decoupled magnetic properties show clear in-plane magnetic anisotropy, pointing to the important role of the unidirectional CDW distortion in breaking the C_4 crystal symmetry. Based on the magnetic properties measured along $H//c$ of 11 different compositions, we also report an Sb-composition-dependent phase diagram. Interestingly, the idealized nonsymmorphic Dirac semimetal $GdSb_{0.46}Te_{1.48}$ is found to exhibit an anoma-

*lschoop@princeton.edu

lously enhanced magnetic susceptibility in a narrow *H-T* phase regime. We discuss the possibility that this is a signature of an antiferromagnetic skyrmion phase. Overall, the rich magnetic phase diagrams are linked to the magnetocrystalline anisotropy and its delicate competition with other energy contributions. In order to understand the role of the out-of-plane magnetic exchange interaction for potential skyrmion formation, we also report the magnetic phase diagram of the antiferromagnetic van der Waals material $GdTe_3$, whose crystal structure features a similar CDW distorted square-net lattice and puckered GdTe bilayers but exhibits fewer and weaker out-of-plane exchange couplings.

II. METHODS

Single crystals of $GdSb_xTe_{2-x-\delta}$ were grown by chemical vapor transport, using iodine as the transport agent. For more details of the growth conditions, see Ref. [9]. By varying the amount of Sb in the starting materials, a series of $GdSb_xTe_{2-x-\delta}$ single crystals with varying Sb content was obtained. The elemental composition was analyzed by energy-dispersive x-ray spectroscopy (EDX) using a Verios 460 scanning electron microscope with an Oxford energy-dispersive x-ray spectrometer and with incident electron energy of 15 keV. Single crystals of $GdTe_3$ were grown by a self-flux method with excess of tellurium. The growth condition was the same as described in Ref. [18]. The magnetic properties were analyzed by a Quantum Design PPMS DynaCool system via the vibrating sample magnetometer (VSM) option. For consistency, all the temperature-dependent magnetic measurements were performed in the warming-up process. The magnetic phase diagrams were established by collecting a series of temperature-dependent magnetization curves, with varying fields up to 9 T, in 0.1-T increments. At each specific field, the critical temperatures in the displayed magnetic phase diagrams are established based on the temperature derivative of the DC magnetic susceptibility, $d\chi/dT$. The critical temperatures are determined by the peak/dip locations of the $d\chi/dT$ curve. In this way, the critical temperatures at a series of fixed fields up to 9 T are collected to build the magnetic phase diagrams in the *H-T* space, therefore also providing critical field information. Examples of how critical temperatures were determined at $\mu_0 H = 0.1$ T are shown in Figs. S1(b) and S1(d) in the Supplemental Material [19].

III. RESULTS AND DISCUSSION

A. Magnetic behavior of $GdSb_{0.46}Te_{1.48}$

Two examples of $GdSb_xTe_{2-x-\delta}$ superstructures resolved by single-crystal x-ray diffraction for $x < 0.85$ are shown in Figs. 1(a) and 1(b), which correspond to $GdSb_{0.21}Te_{1.70}$ and $GdSb_{0.45}Te_{1.53}$, respectively [9]. The subcell and CDW direction are also indicated in the figure. Our prior study indicated that the measured effective magnetic moment for all $GdSb_xTe_{2-x-\delta}$ is close to the theoretical free-ion value of 7.94 μ_B for Gd^{3+} with $4f^7$ configuration [9]. Therefore, the ground-state angular momentum of Gd is $J = 7/2$ ($S = 7/2$, $L = 0$). To simplify the discussion, we assume the Gd lattice to be of simple rectangular symmetry. In this case we might assume at least two nearest-neighbor (*nn*) magnetic exchange

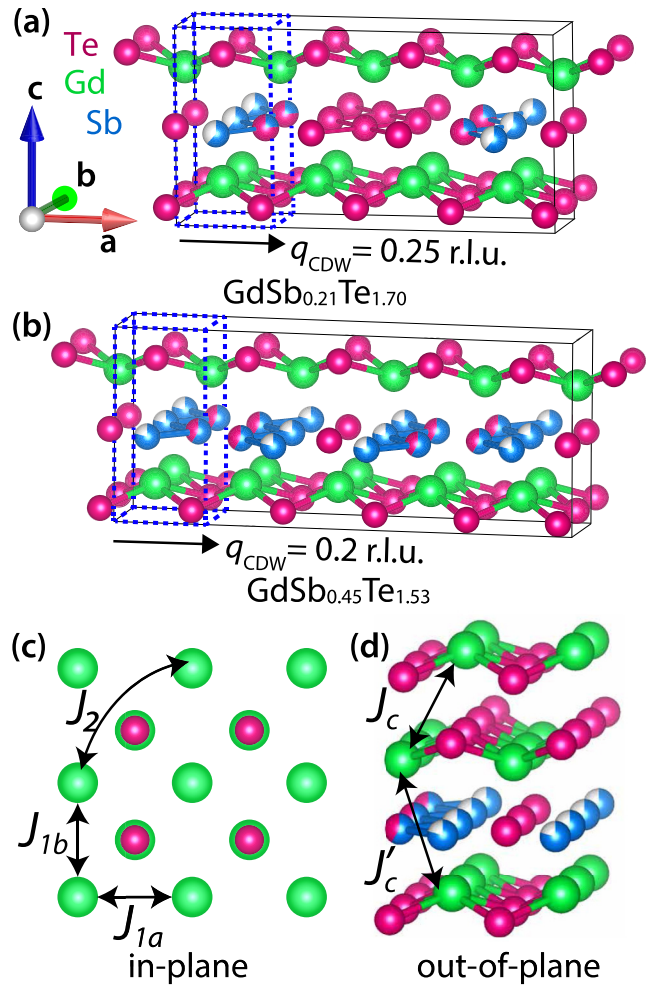

FIG. 1. Two different structures that can be observed in $GdSb_xTe_{2-x-\delta}$ depending on composition [9], as well as the responsible magnetic exchange interactions in a simplified structure. Crystal structures of $GdSb_{0.21}Te_{1.70}$ (a) and $GdSb_{0.45}Te_{1.53}$ (b), with four- and fivefold superstructural modulations, respectively. Solid lines represent the superstructure unit cells. Blue dashed lines indicate the subcell unit cell. The superstructural modulation appears along the *a* axis, as indicated by the black arrows. The CDW wave vectors q_{CDW} are denoted in reciprocal lattice units (r.l.u). Crystal structure solutions are from Ref. [9]. In-plane (c) and out-of-plane (d) magnetic exchange couplings as we assume them to appear in a simplified orthorhombic structure, when ignoring the more complex supercell modulations. Note that J_{1a} and J_{1b} (nearest-neighbor interactions), and J_2 (next-nearest-neighbor interaction) are illustrated as in-plane couplings, while J_c (*nn*) and J_c' (*nnn*) as out-of-plane couplings.

interaction terms, J_{1a} and J_{1b}, and one next-nearest-neighbor (*nnn*) term, J_2, to be responsible for the in-plane magnetic coupling. Since the structure also exhibits two puckered GdTe layers, which are stacked along the *c* axis [Fig. 1(d)], a *nn* out-of-plane coupling, J_c, and a *nnn* out-of-plane coupling, J_c', should also play a role, as we will discuss below. As mentioned in the Introduction, $GdSb_{0.46}Te_{1.48}$ was recently found to be a nearly ideal nonsymmorphic Dirac semimetal with an almost "clean" Dirac node at the Fermi level [15].

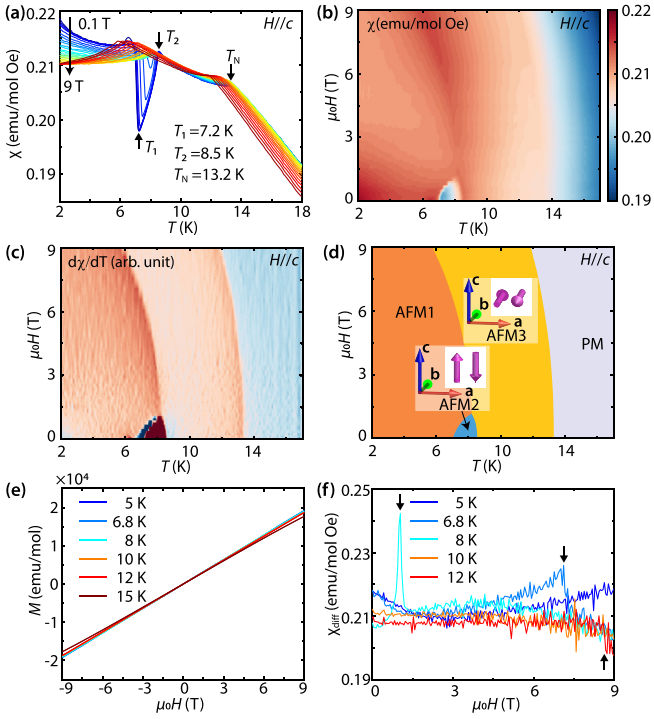

FIG. 2. Magnetic phase diagram of $GdSb_{0.46}Te_{1.48}$ for $H//c$. (a) Temperature-dependent DC magnetic susceptibility (χ) at selected field range from 0.1 to 9 T. The three magnetic transitions at 0.1 T are indicated by the arrows. (b) Map of the DC magnetic susceptibility in the parameter space of magnetic field and temperature. (c) The temperature derivative of the magnetic susceptibility ($d\chi/dT$) shows clear magnetic phase boundaries. (d) The magnetic phase diagram inferred from magnetic susceptibility measurements. PM indicates the paramagnetic phase. AFM1, AFM2, AFM3 are antiferromagnetic phases. The inferred spin orientations for AFM2 and AFM3 phases are also illustrated. (e) Sampled *MH* data at selected temperatures. (f) The differential magnetic susceptibility, $\chi_{\text{diff}} = \mathrm{d}M/\mathrm{d}H$, derived from the *MH* data shown in (e). The field-induced magnetic transitions are indicated by the arrows for the data measured at $T = 6.8$, 8, and 12 K. Note that the magnetic susceptibility data from 2 to 16 K was reported in Ref. [15] and is replotted here in (b) for the convenience of discussion.

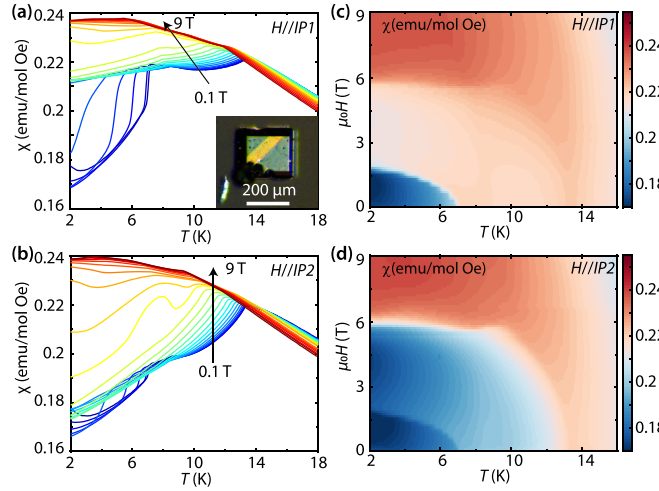

FIG. 3. In-plane magnetic anisotropy of $GdSb_{0.46}Te_{1.48}$. The temperature-dependent DC magnetic susceptibility (χ) at selected field range from 0.1 to 9 T for the two orthogonal in-plane orientations, *IP1* (a) and *IP2* (b). The inset in (a) shows a polarized optical image of a $GdSb_{0.46}Te_{1.48}$ crystal. The bright-dark contrast indicates the two types of CDW domains, whose CDW wave vectors are orthogonal to each other. (c, d) DC magnetic susceptibility maps corresponding to the two in-plane orientations.

For this reason we begin our discussion with the magnetic behavior of $GdSb_{0.46}Te_{1.48}$.

Figure 2 shows the magnetic properties of $GdSb_{0.46}Te_{1.48}$ for $H//c$. The magnetic susceptibility for $\mu_0 H = 0.1$ T reveals three magnetic transitions, $T_1 = 7.2$ K, $T_2 = 8.5$ K, and $T_N = 13.2$ K. Under increasing magnetic field, the temperature window between the T_1 and T_2 transitions gradually shrinks and disappears at a critical field of 1.1 T. Upon further field increase, the magnetic transitions shift to lower temperatures. Figure 2(d) illustrates the magnetic phase diagram. Note that the magnetic phase boundaries are delineated based on the temperature derivative of the magnetic susceptibility, $d\chi/dT$. In a "simple" antiferromagnet where only one antiferromagnetic phase appears, the Néel temperature was suggested to be more accurately described by $d(\chi T)/dT$ [20]. In Fig. S1 in the Supplemental Material [19], we provide the map of $d(\chi T)/dT$ in comparison to Fig. 2(c) and the temperature-dependent curves of $d\chi/dT$ vs $d(\chi T)/dT$ at $\mu_0 H = 0.1$ T. There is no observable difference in the transition temperatures derived by these two methods.

Figure 2(e) shows the *MH* data for field sweeps between –9 and 9 T. The almost linear field-dependent *MH* curves and zero remanent magnetization suggest that the three magnetic ordered phases, AFM1, AFM2, and AFM3, are antiferromagnetic. The field-induced magnetic phase transitions are better revealed in the differential magnetic susceptibility curves [Fig. 2(f)].

To better understand these magnetic phases, we also explored the magnetic properties for fields parallel to the *ab* plane. Since a magnetocrystalline anisotropy is expected for the two in-plane crystallographic axes (*a* and *b* axis shown in Fig. 1), due to the unidirectional CDW distortion, we performed two sets of independent magnetization measurements for either $H//IP1$ or $H//IP2$. The experimental configuration of this magnetic measurement is illustrated in Fig. S3 in the Supplemental Material. The results are shown in Figs. 3(a) and 3(b). *IP1* and *IP2* are aligned to be either parallel or perpendicular to the *a* and *b* axes, respectively. For crystals that undergo a tetragonal-to-orthorhombic structural transition from high to low temperature, ferroelastic structural twinning is often observed in the lower-symmetry phase. In ferroelastic materials, spontaneous strain appears in one of at least two degenerate states (for example, a spontaneous longitudinal strain can appear along the *x* axis or along the *y* axis). Switching can then occur between these degenerate states. Examples for this are the iron arsenide superconductors AFe_2As_2 (A = Ca, Sr, and Ba) [21,22] and $YBa_2Cu_3O_{7-x}$ single crystals [23]. The same happens in the orthorhombic $GdSb_xTe_{2-x-\delta}$ system. The inset of Fig. 3(a) shows a polarized optical image of a $GdSb_{0.46}Te_{1.48}$ crystal with clear ferroelastic twinning. Magnetization measurements on such crystals with fields aligned along either $H//IP1$ or

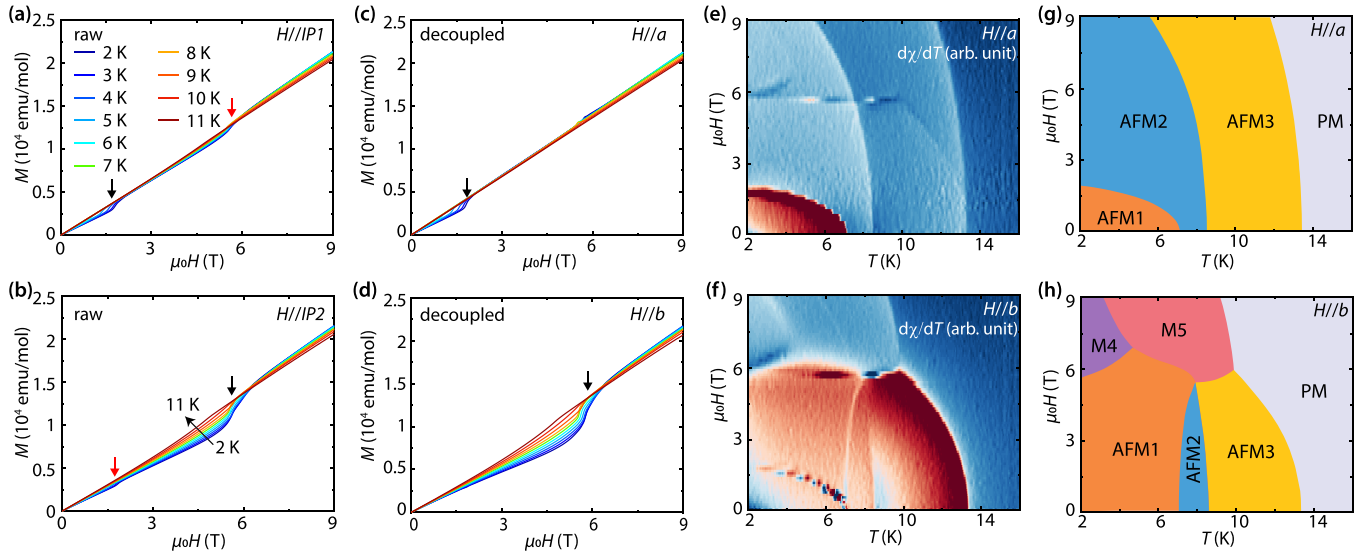

FIG. 4. Magnetic phase diagram of $GdSb_{0.46}Te_{1.48}$ for fields parallel to the two in-plane orientations. *MH* measurements for *H//IP1* (a) and *H//IP2* (b), respectively, from 2 to 11 K. The field-induced magnetic transitions are indicated by arrows. The red arrows indicate the weaker transition feature resulting from domain mixing. Decoupled *MH* data for *H//a* (c) and *H//b* (d), respectively. (e, f) Temperature derivatives of the decoupled magnetic susceptibilities. (g, h) The magnetic phase diagrams for *H//a* and *H//b*, respectively. PM indicates the paramagnetic phase. AFM1, AFM2, and AFM3 are antiferromagnetic phases, as discussed in the main text. M4 and M5 are field-induced magnetic phases

H//IP2 consist of intrinsic magnetic responses from twin domains in which both *H//a* and *H//b* contribute (see Fig. S3 in the Supplemental Material); the weight of each intrinsic response depends on their relative domain volume ratio. If the volume of one type of domain is predominant over the other, the in-plane magnetic anisotropy can still be resolved. The temperature-dependent magnetic susceptibility of $GdSb_{0.46}Te_{1.48}$ for *H//IP1* [Fig. 3(a)] and *H//IP2* [Fig. 3(b)] shows a clear difference below $T_N = 13.2$ K at low field. The difference is also visualized in the magnetic susceptibility map [Figs. 3(c) and 3(d)].

To gain a better understanding of the magnetic anisotropy, we performed further *MH* measurements for fields parallel to *IP1* and *IP2* [Figs. 4(a) and 4(b)]. Two spin-flop transitions can be observed at $\mu_0 H \approx 1.7$ and 5.7 T in the curves measured at $T = 2$ and 3 K, as indicated by the arrows. For measurements on a single crystal that would only consist of a single domain, the intrinsic *MH* data can be formally described as a function, $M_a(H)$ for *H//a* and $M_b(H)$ for *H//b*. If mixed domains are present, the measured magnetization can be considered as a simple summation of the magnetization for the two species of domains (the negligible response from the domain wall region is ignored):

$$M_{IP1}(H) = \lambda M_a(H) + (1-\lambda) M_b(H), \quad (1)$$

$$M_{IP2}(H) = \lambda M_b(H) + (1-\lambda) M_a(H), \quad (2)$$

where M_{IP1} and M_{IP2} denote the magnetization measured along *IP1* and *IP2* orientations, respectively, and λ describes the volume fraction of the *a* domain, in which the *a* axis is parallel to *IP1* orientation. For $\lambda = 1$, the measurement for *H//IP1* is equivalent to *H//a*. From Eqs. (1) and (2), the intrinsic magnetic response $M_a(H)$ and $M_b(H)$ can be derived:

$$M_a(H) = \frac{-\lambda}{1-2\lambda} M_{IP1}(H) + \frac{1-\lambda}{1-2\lambda} M_{IP2}(H), \quad (3)$$

$$M_b(H) = \frac{1-\lambda}{1-2\lambda} M_{IP1}(H) + \frac{-\lambda}{1-2\lambda} M_{IP2}(H). \quad (4)$$

Once λ is known, the intrinsic magnetic response without a domain mixing effect can be obtained even though the measurements were performed on a crystal with CDW twin domains. Here we utilize the features of the field-induced spin-flop transitions at $\mu_0 H \approx 1.7$ and 5.7 T [Figs. 4(a) and 4(b)] to evaluate λ. A detailed description of the *MH*-data decoupling is provided in the Supplemental Material. The intrinsic *MH* response after decoupling is shown in Figs. 4(c) and 4(d).

Up to this stage, we have obtained two sets of intrinsic *MH* data corresponding to field conditions of *H//a* and *H//b*. However, which set of *MH* curves corresponds to which field orientation is still unknown. To address this we took advantage of mechanical detwinning. For orthorhombic crystals with in-plane ferroelastic twinning, external mechanical stress can tune the domain population [24,25]. For orthorhombic $GdSb_xTe_{2-x-\delta}$, the subcell lattice parameter *a* along the CDW wave-vector direction, is larger than the other in-plane parameter *b*. Therefore uniaxial compressive stress along either in-plane crystallographic axis is able to facilitate the preferential growth of domains that have the short *b* axis along the stress direction. Such mechanical approach has been used before to detwin AFe_2As_2 (A = Ca, Sr, and Ba) single crystals [21,22]. We successfully mechanically detwinned a $GdSb_{0.53}Te_{1.44}$, which has a slightly different composition from $GdSb_{0.46}Te_{1.48}$. Nevertheless, the overall magnetic phases are quite similar between those two

compositions, as evidenced by their similar temperature and field-induced magnetic phase transitions in measured $\chi(T)$ curves [Figs. 3(a) and 3(b) vs Fig. S6(d)], and $M(H)$ [Figs. 4(a) and 4(b) vs Fig. S6(c)]. Therefore the measured in-plane magnetic anisotropy of detwinned $GdSb_{0.53}Te_{1.44}$ is used to establish the in-plane magnetic anisotropy of $GdSb_{0.46}Te_{1.48}$. With mechanical detwinned crystals, we can conclude that the spin-flop transitions at $\mu_0 H \approx 1.7$ and 5.7 T correspond to $H//a$ and $H//b$, respectively, as indicated in Figs. 4(c) and 4(d). Our mechanical detwinning experiment demonstrates that the spontaneously strained state in the orthorhombic $GdSb_xTe_{2-x-\delta}$ can indeed be switched, i.e., the CDW wave vector can undergo a 90° switch. More details on the mechanical twinning are provided in the Supplemental Material. Using the same MH decoupling procedure as described above, we could derive the resulting magnetic phase diagrams for $H//a$ and $H//b$ [Figs. 4(e) and 4(f)].

We now discuss the orientation of the magnetic moment in the different magnetic ordered phases. Since Gd strongly absorbs neutrons, it is difficult to determine the magnetic structure with neutron diffraction. Nevertheless, we are able to gain some insight on the nature of the magnetic phases based on the magnetic susceptibility measured along the three principal crystallographic orientations [χ_c in Fig. 2(a), decoupled χ_a and χ_b in Fig. S4 in the Supplemental Material]. At T_N, there is a peak in χ_b, while χ_c and χ_a become relatively flat for $T_2 < T < T_N$; thus the spins in the AFM3 phase are clearly oriented along the b axis [illustrated in Fig. 2(d)]. For $T_1 < T < T_2$, there is a sharp drop in χ_c, in contrast to a subtle change in the slope of χ_a and χ_b. This implies a spin-reorientation transition to a new antiferromagnetic phase [AFM2, illustrated in Fig. 2(d)], with the spins flopping from the b to the c axis. Below T_1, χ_c sharply recovers from the dip and remains relatively flat down to the lowest measured temperature, while χ_a sharply drops, and both χ_a and χ_b continuously decrease upon cooling. This suggests another spin-reorientation transition into an antiferromagnetic state, with the spins flopping from the c to the ab plane. Since χ_a and χ_b show a similar temperature-dependent behavior down to the lowest measured temperature, the magnetic easy axis of the AFM1 phase may point to an in-plane orientation other than a or b axes, or the AFM1 phase exhibits a spiral spin texture with magnetic moments lying in the ab plane.

At higher fields, field-induced magnetic phases, M4 and M5, appear for $H//b$ [Fig. 4(h)]. Since the MH curves are still linear and the extrapolation of the magnetization down to zero field is nearly zero, we conclude that M4 and M5 are likely also antiferromagnetic phases, where the moments are net canted along the b axis. Considering the characteristic spin-flop transitions at $\mu_0 H \approx 5.7$ T, both M4 and M5 phases are likely to have their antiferromagnetic spin component oriented along the a axis, although their respective antiferromagnetic spin configurations are different.

We next focus on the low-field behavior of $GdSb_{0.46}Te_{1.48}$. Figure 5(a) shows $\chi_c(T)$ for a field range from 40 to 3000 Oe. An anomalously enhanced χ_c is observed in the temperature range of 6.2 K $< T <$ 7.0 K. The anomalous behavior is better revealed in the magnetic susceptibility map [Fig. 5(b)], where the anomalous region is surrounded by the AFM1 and AFM2 phases. Since the AFM1 and AFM2 phases were concluded

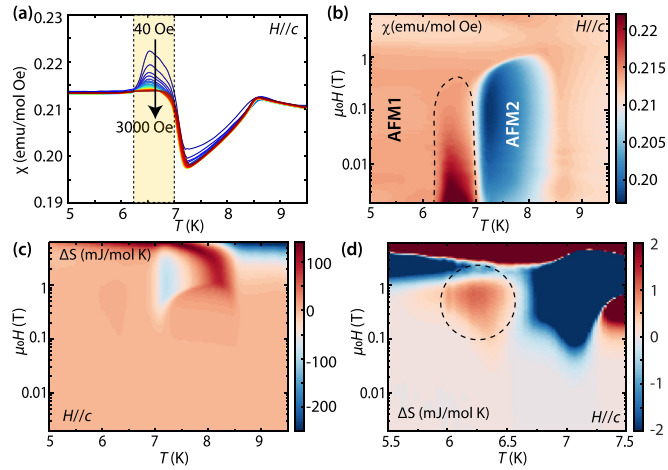

FIG. 5. Low-field magnetic behavior of $GdSb_{0.46}Te_{1.48}$ for $H//c$. (a) Temperature-dependent DC magnetic susceptibility (χ) at a selected field range from 40 to 3000 Oe. The temperature window where χ shows anomalous enhancement is indicated by the shaded rectangle. (b) The low-field magnetic susceptibility map. The region with enhanced magnetic susceptibility is outlined by the dashed line. (c) Map of the relative magnetic entropy, ΔS. (d) Zoom-in rescaled relative magnetic entropy. The region with enhanced ΔS is indicated by the dashed circle. Note that the vertical axes in (b–d) are plotted in a log scale.

to have an in-plane and out-of-plane spin orientation, respectively, the phase regime in between is of particular interest: the in-plane and out-of-plane magnetic anisotropy energy are expected to have a delicate balance. A noncollinear spin texture could be a likely consequence. One possibility could be the appearance of skyrmions [26–28], which are particlelike spin textures of topological origin.

One signature of a skyrmion phase can be revealed by a magnetoentropic analysis, as demonstrated by the recent studies on FeGe [29] and $Co_8Zn_9Mn_3$ [30]. Formally, the magnetic entropy change $\Delta S_M(T,H)$ is expressed as

$$\Delta S_M(T,H) = S_M(T,H) - S_M(T,0) = \int_0^H \left[\frac{\partial S(T,H)}{\partial H}\right]_T dH, \quad (5)$$

where S is the total entropy. With Maxwell's relation $[\partial S(T,H)/\partial H]_T = [\partial M(T,H)/\partial T]_H$, the equation above can be rewritten as

$$\Delta S_M(T,H) = \int_0^H \left[\frac{\partial M(T,H)}{\partial T}\right]_H dH. \quad (6)$$

Therefore the magnetocaloric response of a skyrmion host can be experimentally evaluated by a series of $M(T)$ measurements under different applied magnetic fields. To visualize the field-induced isothermal magnetic entropy change in the H-T space, the entropy $\Delta S_M(T,H)$ at zero field is considered as a baseline and $\Delta S_M(T,0)$ is set to zero. Figure 5(c) shows the map of $\Delta S_M(T,H)$ obtained using Eq. (6). Figure 5(d) shows the rescaled zoom-in view, highlighting the enhanced entropy region (outlined by the dashed circle). Such a feature is similar to that observed in FeGe [29] and $Co_8Zn_9Mn_3$ [30], with an

enhanced entropy in the skyrmion lattice regime relative to the neighboring phases.

The existence of skyrmions in magnetic materials is usually a result of a delicate interplay between different energy terms [31]. So far the majority of known skyrmion-hosting materials are noncentrosymmetric, and the critical energy term that is responsible for the noncollinear spin texture of skyrmions is the Dzyaloshinskii-Moriya (DM) interaction [32,33].

However, it has been theoretically proposed that frustrated exchange interactions [34–36] and higher-order coupling beyond the Ruderman-Kittel-Kasuya-Yosida (RKKY) interaction [37,38] are two possible mechanisms to introduce skyrmions in a centrosymmetric material. For the former mechanism, both triangular and square lattices were discussed due to the competition of *nn* interaction and further *nn* interactions. For the latter, the effective multiple spin coupling beyond the conventional RKKY interaction is the key ingredient for stabilization of the skyrmion phase in itinerant electron systems with local magnetic moments. Soon after these theoretical proposals, the emergence of a skyrmion state in a centrosymmetric material was experimentally discovered in the frustrated metallic magnets, Gd_2PdSi_3 (Gd forms a layered triangular lattice) [39], $Gd_3Ru_4Al_{12}$ (Gd forms a layered distorted kagome lattice) [40], and $GdRu_2Si_2$ (Gd forms a layered square net) [41]. The origin of skyrmions in these materials was linked to these proposed mechanisms. In $GdSb_{0.46}Te_{1.48}$, we believe that these two mechanisms are both active, which lays the foundation for a possible existence of a skyrmion phase. Below we list three aspects of magnetic properties that are similar to these three centrosymmetric skyrmion materials, especially $GdRu_2Si_2$.

First, all these systems feature the large local magnetic moment from Gd with $J = 7/2$, which is expected to be minimally affected by thermal fluctuations. This suggests that thermal fluctuations may not play as important of a role as in chiral magnets. Indeed, the region of interest in the *H-T* phase diagram for all these systems is located at relatively low temperatures ($T < \sim$20 K for Gd_2PdSi_3, $T < \sim$13 K for $Gd_3Ru_4Al_{12}$, $T < \sim$20 K for $GdRu_2Si_2$, and $T < 6.7$ K for $GdSb_{0.46}Te_{1.48}$). Theoretically, it was found that the skyrmion phase in a metallic centrosymmetric material can be stabilized as a ground state ($T = 0$) by contributions that are higher order than the conventional RKKY interactions [37].

Second, all these systems are metallic, and they show frustrations to a certain degree. In a square lattice, frustration comes from the *nn* interaction competing with additional longer-range interaction (including the *nnn* interactions) [36]. Fundamentally, the RKKY coupling, which oscillates as a function of Gd-Gd distance, is likely the origin of the frustration, similar to that in $Gd_3Ru_4Al_{12}$ [40,42], Gd_2PdSi_3 [39], and $GdRu_2Si_2$ [43,44]. The competition in magnetic interactions leads to the formation of many magnetic phases in the *H-T* phase diagram, as was demonstrated in all four systems. A skyrmion phase in almost all known bulk materials features a narrow phase region, which is neighboring multiple magnetic phases in the *H-T* diagram. The small energy difference between these neighboring phases lays the foundation for the formation of skyrmion phase.

Third, superstructures are found in the zero-field magnetic ordered phases in all four systems. In the case of Gd_2PdSi_3, the crystal structure itself is characterized by a 2×2 enlargement of the unit cell in the hexagonal basal plane and an eightfold enlargement along the out-of-plane direction [39,45]. The ground-state magnetic order is characterized by an incommensurate noncoplanar spin texture. In the case of $Gd_3Ru_4Al_{12}$, spins form an incommensurate helical order at the ground state [40]. In the case of $GdRu_2Si_2$, an incommensurate screw magnetic structure was determined as the ground state [41]. Recently, a charge density modulation arising from the coupling between itinerant electron states and local magnetic moments has also been observed by scanning tunneling microscopy [46]. For $GdSb_{0.46}Te_{1.48}$, a single-crystal x-ray diffraction (XRD) analysis indicated a fivefold superstructure along one of the in-plane lattice orientations. However, considering the possible limited q resolution of instrument and the tunable CDW wave vector in the $GdSb_xTe_{2-x-\delta}$ series [9], an incommensurate structure is also possible. With strong magnetoelastic coupling, the ground-state AFM1 phase is likely to have an incommensurate noncollinear magnetic order, as mentioned above.

In addition to the aforementioned similarities to some known skyrmion materials, $GdSb_{0.46}Te_{1.48}$ also exhibits some distinct magnetic properties. The neighboring phases of the anomalous region in $GdSb_{0.46}Te_{1.48}$ [Fig. 5(d)] are antiferromagnetic, in contrast to the typical field-aligned ferromagnetic (FA-FM) or paramagnetic (PM) neighboring phases in many skyrmion materials, including centrosymmetric and noncentrosymmetric ones. Examples include the aforementioned Gd_2PdSi_3 (PM) [39], FeGe (FA-FM) [27], MnSi (FA-FM or PM) [26], and $Co_8Zn_9Mn_3$ (PM) [30,47], as well as other compounds, such as $VOSe_2O_5$ (PM) [48], $Fe_{0.5}Co_{0.5}Si$ (FA-FM) [49], and Cu_2OSeO_3 (PM) [50,51], with well-defined phase diagrams. Therefore, if a skyrmion phase in $GdSb_{0.46}Te_{1.48}$ is present, it would likely be of a different type, for example, it could be an antiferromagnetic skyrmion phase.

The concept of antiferromagnetic skyrmions was developed a few years ago [52,53], but it has been mainly limited to theoretical studies so far [54–58]. In fact, antiferromagnetic skyrmions have not been experimentally observed in bulk materials yet, to the best of our knowledge. The difficulty in identifying promising materials that host antiferromagnetic skyrmions might be related to the vanishing skyrmion Hall effect, as is concluded from both the analytical theory and micromagnetic simulations [52–55,57,59]. Such behavior prevents an efficient screening of candidate materials by electrical transport measurements. Antiferromagnetic skyrmions can be considered as two coupled ferromagnetic skyrmions with opposite topological winding numbers due to the presence of antiferromagnetic exchange interactions; therefore, the winding number of an antiferromagnetic skyrmion is zero. Experimentally, we did not observe a nonzero topological Hall effect in $GdSb_{0.46}Te_{1.48}$, which indicates either the absence of skyrmions or the presence of antiferromagnetic skyrmions. Since the antiferromagnetic exchange interaction is a necessary ingredient, antiferromagnets are naturally the candidates in which to look for antiferromagnetic skyrmions. Based on the discussion above, we expect $GdSb_{0.46}Te_{1.48}$ to be a promising candidate.

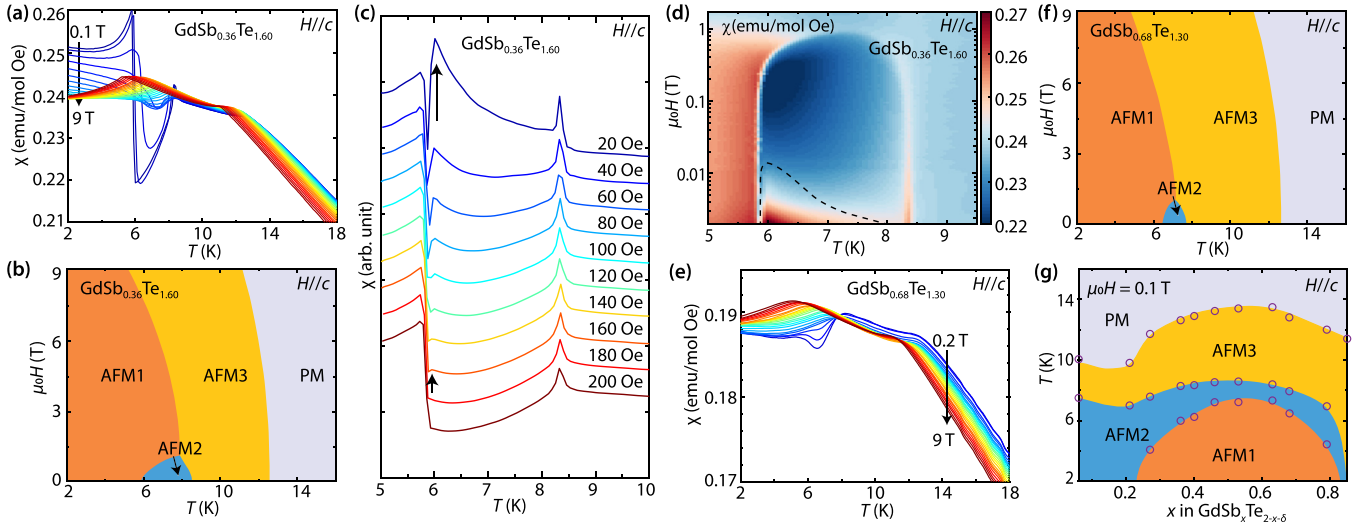

FIG. 6. Magnetic properties of $GdSb_xTe_{2-x-\delta}$ with varying composition. (a) Temperature-dependent DC magnetic susceptibility of $GdSb_{1.36}Te_{1.60}$ at a selected field range of 0.1–9 T, and (b) the corresponding phase diagram. (c) Temperature-dependent DC magnetic susceptibility of $GdSb_{1.36}Te_{1.60}$ at low fields from 20 to 200 Oe, and (d) the corresponding magnetic susceptibility map. Arrows in (c) indicate anomalously enhanced χ_c. The feature maintains for fields up to 180 Oe. The region with anomalously enhanced χ_c in (d) is outlined by the dashed line. (e) Temperature-dependent DC magnetic susceptibility of $GdSb_{1.68}Te_{1.30}$ at a selected field range of 0.1–9 T, and (f) the corresponding phase diagram. (g) Evolution of the low-field magnetic phases with respect to Sb composition. AFM1, AFM2, and AFM3 indicate three antiferromagnetic phases, as discussed in the main text. The circles indicate the three-phase transition boundaries extracted from $\chi_c(T)$ at $\mu_0 H = 0.1\,T$. Note that the possible skyrmion phase observed in $GdSb_{0.46}Te_{1.48}$ is not marked in the diagram, as the anomalous response in χ_c was not observed in the compounds with neighboring Sb compositions ($GdSb_{0.40}Te_{1.54}$ and $GdSb_{0.53}Te_{1.44}$) when $\mu_0 H = 0.1$ T.

B. Magnetic properties of $GdSb_xTe_{2-x-\delta}$ with other compositions

To better understand how stable the potential skyrmion region is in the $GdSb_xTe_{2-x-\delta}$ system, we additionally studied $GdSb_xTe_{2-x-\delta}$ compounds with Sb contents below and above 0.46.

Figures 6(a) and 6(b) show the temperature-dependent DC magnetic susceptibilities under fields up to 9 T ($H//c$) and the magnetic phase diagram of $GdSb_{0.36}Te_{1.60}$, respectively. Overall, $GdSb_{0.36}Te_{1.60}$ has similar magnetic properties to $GdSb_{0.46}Te_{1.48}$. Three magnetic phases, AFM1, AFM2, and AFM3, can be identified. The shapes of these phase regions in the H-T diagram are similar to those of $GdSb_{0.46}Te_{1.48}$ [Fig. 2(d)], except that the phase region of AFM2 moves to slightly lower temperature, and it exists at a wider temperature range at low fields. For the AFM1 phase, we found that the magnetic susceptibility at low field ($\mu_0 H = 0.1$ T) is significantly larger than that at high field, which is different from $GdSb_{0.46}Te_{1.48}$. This indicates a stronger polarizability along the c axis for the low-field AFM1 phase of $GdSb_{0.36}Te_{1.60}$ compared to the same phase in $GdSb_{0.46}Te_{1.48}$.

Notably is the low-field magnetic behavior of $GdSb_{0.36}Te_{1.60}$ in comparison with $GdSb_{0.46}Te_{1.48}$. Figure 6(c) shows the temperature-dependent DC magnetic susceptibility under fields up to 200 Oe. Within the AFM2 phase region, anomalous peaks can be resolved for fields up to 180 Oe. This region is highlighted in Fig. 6(d). The existence of such a region with enhanced low-field susceptibility might share the same origin as that in $GdSb_{0.46}Te_{1.48}$, although the former region is within the AFM2 phase while the latter one is within the AFM1 phase. The appearance of such a region in two different phases indicates a change of energy landscape in magnetic interactions, upon a change in Sb/Te ratio.

Moving to compounds with higher Sb composition, we show the temperature-dependent DC magnetic susceptibilities and the H-T phase diagram of $GdSb_{0.68}Te_{1.30}$ in Figs. 6(e) and 6(f), respectively. Although all three magnetic phases are still observed, the phase space of AFM2 is getting smaller. Additionally, the low-field magnetic susceptibility of the AFM1 phase is clearly smaller than the high-field one [Fig. 6(e)]. We do not observe any regions with anomalously enhanced low-field susceptibility in $GdSb_{0.68}Te_{1.30}$, in contrast to that in $GdSb_{0.36}Te_{1.60}$ and $GdSb_{0.46}Te_{1.48}$.

In Fig. 6(g) we summarize the magnetic phase evolution in respect to the Sb content (x) ($\mu_0 H = 0.1\,T$). The phase regions of AFM1, AFM2, and AFM3 are all dome-shaped, and the phase transition temperatures summit when $x \sim 0.55$–0.60. Additionally, the AFM1 phase disappears at both the low-x and high-x limit.

The increase of the AFM3-AFM2 and AFM2-AFM1 transition temperatures upon decrease in x on the high-x side of the T-x diagram is related to the development of CDW distortion that breaks the C_4 symmetry and the gradual increase of the a/b ratio [9]. In this sense, the formation of the AFM1 and AFM2 phases should be related to the emergence of an in-plane magnetocrystalline anisotropy when $x < 0.85$. However, the orthorhombic distortion might not be the only factor that affects the stability of the AFM1 and AFM2 phases, because the maximum transition temperatures appear at $x \sim 0.55$–0.60, while the maximum a/b ratio occurs at $x \sim 0.25$ [9]. This implies the contributions from other

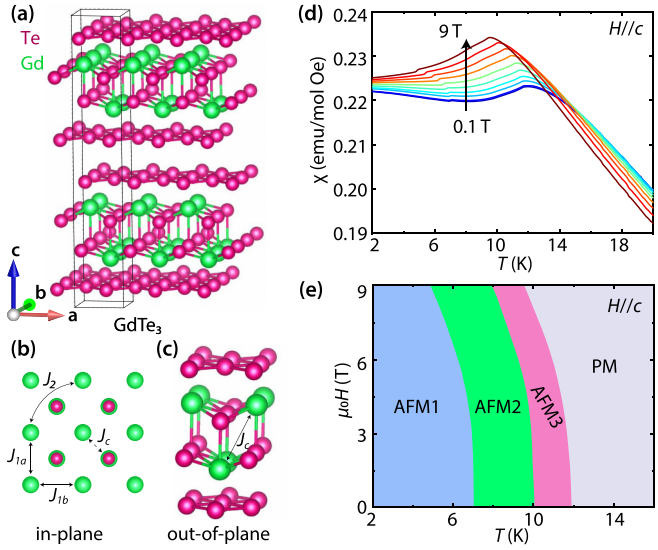

FIG. 7. Magnetic phase diagram of $GdTe_3$. (a) Illustration of crystal structure of $GdTe_3$. In-plane (b) and out-of-plane (c) exchange coupling terms. (d) Temperature-dependent DC magnetic susceptibility at a selected field range of 0.1–9 T for fields along the out-of-plane orientation. (e) Magnetic phase diagrams for $H//c$. PM indicates paramagnetic phase. AFM1, AFM2, and AFM3 are antiferromagnetic phases, as discussed in the main text.

energy terms. For a metallic antiferromagnet, this could be from long-range RKKY interactions. The RKKY interaction is sensitive to the density of states because it depends on the number of electrons contributing to the spin exchange. With decrease in x, the crystal structure of $GdSb_xTe_{2-x-\delta}$ tends to distort more, eventually leading to a reduction in the number of conducting electrons to interact with the local spins, which likely disfavors the formation of AFM1 and AFM2 phases.

On the low-x ($x <\sim 0.2$) side of the phase diagram shown in Fig. 6(g), the PM-AFM3 and AFM3-AFM2 transition temperatures appear to slightly increase with lower x. This might be related to the structural transition from a unidirectional CDW distortion to a bidirectional one, when x is reduced to below ~0.2 [9].

C. Magnetic properties of $GdTe_3$

As discussed above, we can tentatively consider several in-plane magnetic exchange interactions, including two anisotropic *nn* interactions (J_{1a} and J_{1b}) and the *nnn* nearest interaction (J_2) (Fig. 1), which might be responsible for the many magnetically ordered phases observed in $GdSb_xTe_{2-x-\delta}$. However, out-of-plane magnetic exchange interactions (J_c and J_c'), could also play a role. In order to test whether out-of-plane exchange interactions are important for the potential appearance of skyrmions, we investigated a structurally related, more two-dimensional material, $GdTe_3$.

The structure of $GdTe_3$, without accounting for the CDW, is illustrated in Fig. 7(a). Just as $GdSb_xTe_{2-x-\delta}$ ($\sim 0.20 < x < 0.85$), $GdTe_3$ also features unidirectional-CDW-distorted square lattices. Therefore, we expect similar in-plane magnetic exchange interaction terms [Fig. 7(b)] as in $GdSb_xTe_{2-x-\delta}$. However, the structural difference along the out-of-plane direction should lead to different out-of-plane exchange interactions. Each GdTe bilayer is separated by two square-lattice planes in $GdTe_3$ but only one in $GdSb_xTe_{2-x-\delta}$. Therefore the interbilayer magnetic exchange interaction (J_c') in $GdTe_3$ is expected to be significantly weaker than that in $GdSb_xTe_{2-x-\delta}$, and only the intrabilayer out-of-plane exchange interaction (J_c) is considered to be a dominant term [Fig. 7(c)].

Figures 7(d) and 7(e) show the temperature-dependent DC magnetic susceptibility [$\chi_c(T)$] and the H-T phase diagram for $H//c$. The low-field susceptibility $\chi_c(T)$ remains fairly flat down to the lowest measured temperature below T_N, which is different from $GdSb_{0.46}Te_{1.48}$, where the susceptibility dips [Fig. 2(a)]. Therefore, at least the AFM2 phase should be different between these two materials. We expect an in-plane magnetic easy axis for all three magnetically ordered phases in $GdTe_3$.

Because of the structural difference, we can link the difference in the magnetic phase diagrams between $GdTe_3$ and $GdSb_xTe_{2-x-\delta}$ to the interbilayer out-of-plane exchange coupling term, J_c', in $GdSb_xTe_{2-x-\delta}$. In the discussion above, we have considered the roles of the in-plane *nnn* interactions in competition with the *nn* interaction term in the formation of the complex magnetic phases. Based on the comparison with $GdTe_3$, it can be concluded that the out-of-plane exchange interaction, particularly the interbilayer out-of-plane exchange coupling term, also plays an important role for the formation of magnetic phases with an out-of-plane easy axis and therefore also affects the potential existence of a skyrmion phase.

IV. CONCLUSION AND OUTLOOK

In this work we have reported the magnetic properties of square-lattice-based, topological semimetal candidates $GdSb_xTe_{2-x-\delta}$. For one composition, $GdSb_{0.46}Te_{1.48}$, we reported the magnetic phase diagrams for three different field orientations. At low fields we found an anomalous region in the H-T phase diagram with enhanced magnetic susceptibility, which hints towards the existence of antiferromagnetic skyrmions. To understand the rich magnetic phases, we qualitatively analyzed the roles of *nn* and *nnn* in-plane magnetic exchange interactions, and intrabilayer and interbilayer out-of-plane exchange interactions by studying a structurally related, more two-dimensional material. Frustrated RKKY interactions and higher-order coupling beyond the RKKY interactions are the two fundamental motifs contributing to the competition of these terms in $GdSb_xTe_{2-x-\delta}$ and might lead to an antiferromagnetic skyrmion phase in $GdSb_{0.46}Te_{1.48}$. In this context, we would like to mention RMn_2Ge_2 (R = La, Ce, Pr, and Nd) with a Mn square lattice. Here, the Mn^{2+} forms a high spin state that is largely localized. In this system it was argued that the long-range RKKY interactions via mobile electrons are a primary source for the out-of-plane Mn-Mn coupling, giving rise to frustrated interactions and the conical spin order [60].

More broadly, we believe the square-lattice system of $LnSb_xTe_{2-x-\delta}$ presents an outstanding platform to investigate the rich physics endowed by complex magnetism,

CDWs, Dirac semimetal states, and their possible interplay. The possible existence of an antiferromagnetic skyrmion in the same phase that was shown to be an ideal nonsymmorphic Dirac semimetal, makes this family of materials even more appealing, as antiferromagnetic skyrmions have not been experimentally observed in any bulk materials before. Our results therefore point to the existence of antiferromagnetic skyrmions in an ideal Dirac semimetal.

ACKNOWLEDGMENTS

This research was supported by the Arnold and Mabel Beckman Foundation through a Beckman Young Investigator grant awarded to L.M.S, and the Princeton Center for Complex Materials, a National Science Foundation (NSF)-MRSEC program (DMR-2011750). The authors acknowledge the use of Princeton's Imaging and Analysis Center, which is partially supported by the Princeton Center for Complex Materials.

[1] S. Klemenz, A. K. Hay, S. M. L. Teicher, A. Topp, J. Cano, and L. M. Schoop, The role of delocalized chemical bonding in square-net-based topological semimetals, J. Am. Chem. Soc. **142**, 6350 (2020).

[2] L. M. Schoop, M. N. Ali, C. Straßer, A. Topp, A. Varykhalov, D. Marchenko, V. Duppel, S. S. Parkin, B. V. Lotsch, and C. R. Ast, Dirac cone protected by non-symmorphic symmetry and three-dimensional Dirac line node in ZrSiS, Nat. Commun. **7**, 1 (2016).

[3] S. Klemenz, S. Lei, and L. M. Schoop, Topological semimetals in square-net materials, Annu. Rev. Mater. Res. **49**, 185 (2019).

[4] L. M. Schoop, A. Topp, J. Lippmann, F. Orlandi, L. Müchler, M. G. Vergniory, Y. Sun, A. W. Rost, V. Duppel, M. Krivenkov, S. Sheoren, P. Manuael, A. Varykhalov, B. Yan, R. K. Kremer, R. Ast, Christian, and B. V. Lotsch, Tunable Weyl and Dirac states in the nonsymmorphic compound CeSbTe, Sci. Adv. **4**, eaar2317 (2018).

[5] A. Topp, M. G. Vergniory, M. Krivenkov, A. Varykhalov, F. Rodolakis, J. McChesney, B. V. Lotsch, C. R. Ast, and L. M. Schoop, The effect of spin-orbit coupling on nonsymmorphic square-net compounds, J. Phys. Chem. Solids **128**, 296 (2019).

[6] M. M. Hosen, G. Dhakal, K. Dimitri, P. Maldonado, A. Aperis, F. Kabir, C. Sims, P. Riseborough, P. M. Oppeneer, D. Kaczorowski, T. Durakiewicz, and M. Neupane, Discovery of topological nodal-line fermionic phase in a magnetic material GdSbTe, Sci. Rep. **8**, 13283 (2018).

[7] R. Sankar, I. P. Muthuselvam, K. R. Babu, G. S. Murugan, K. Rajagopal, R. Kumar, T.-C. Wu, C.-Y. Wen, W.-L. Lee, G.-Y. Guo, and F.-C. Chou, Crystal growth and magnetic properties of topological nodal-line semimetal GdSbTe with antiferromagnetic spin ordering, Inorg. Chem. **58**, 11730 (2019).

[8] A. Weiland, D. G. Chaparro, M. G. Vergniory, E. Derunova, J. Yoon, I. W. Oswald, G. T. McCandless, M. Ali, and J. Y. Chan, Band structure engineering of chemically tunable LnSbTe (Ln= La, Ce, Pr), APL Mater. **7**, 101113 (2019).

[9] S. Lei, V. Duppel, J. M. Lippmann, J. Nuss, B. V. Lotsch, and L. M. Schoop, Charge density waves and magnetism in topological semimetal candidates $GdSb_xTe_{2-x-\delta}$, Adv. Quantum Technol. **2**, 1900045 (2019).

[10] K. Pandey, R. Basnet, A. Wegner, G. Acharya, M. R. U. Nabi, J. Liu, J. Wang, Y. K. Takahashi, B. Da, and J. Hu, Electronic and magnetic properties of the topological semimetal candidate NdSbTe, Phys. Rev. B **101**, 235161 (2020).

[11] S. Yue, Y. Qian, M. Yang, D. Geng, C. Yi, S. Kumar, K. Shimada, P. Cheng, L. Chen, Z. Wang, H. Weng, Y. S. Shi, K. Wu, and B. Feng, Topological electronic structure in the antiferromagnet HoSbTe, Phys. Rev. B **102**, 155109 (2020).

[12] L. Šmejkal, Y. Mokrousov, B. Yan, and A. H. MacDonald, Topological antiferromagnetic spintronics, Nat. Phys. **14**, 242 (2018).

[13] E. DiMasi, B. Foran, M. C. Aronson, and S. Lee, Stability of charge-density waves under continuous variation of band filling in $LaTe_{2-x}Sb_x$ $(0 < x < 1)$, Phys. Rev. B **54**, 13587 (1996).

[14] S. M. Young and C. L. Kane, Dirac Semimetals in Two Dimensions, Phys. Rev. Lett. **115**, 126803 (2015).

[15] S. Lei, S. M. L. Teicher, A. Topp, K. Cai, J. Lin, F. Rodolakis, J. L. McChesney, M. Krivenkov, D. Marchenko, A. Varykhalov, C. R. Ast, R. Car, J. Cano, M. G. Vergniory, O. N. Phuan, and L. M. Schoop, Charge density waves as a tool for creating idealized (magnetic) topological semimetals, arXiv:2009.00620.

[16] M. Koshino and I. F. Hizbullah, Magnetic susceptibility in three-dimensional nodal semimetals, Phys. Rev. B **93**, 045201 (2016).

[17] G. P. Mikitik and Y. V. Sharlai, Magnetic susceptibility of topological nodal semimetals, Phys. Rev. B **94**, 195123 (2016).

[18] S. Lei, J. Lin, Y. Jia, M. Gray, A. Topp, G. Farahi, S. Klemenz, T. Gao, F. Rodolakis, J. L. McChesney, C. R. Ast, A. Yazdani, K. S. Burch, S. Wu, N. P. Ong, and L. M. Schoop, High mobility in a van der Waals layered antiferromagnetic metal, Sci. Adv. **6**, eaay6407 (2020).

[19] See Supplemental Material at http://link.aps.org/supplemental/10.1103/PhysRevB.103.134418 for examples of how critical temperatures were determined by $d\chi/dT$ vs. $d(\chi T)/dT$.

[20] M. E. Fisher, Relation between the specific heat and susceptibility of an antiferromagnet, Philos. Mag. **7**, 1731 (1962).

[21] M. A. Tanatar, E. C. Blomberg, A. Kreyssig, M. G. Kim, N. Ni, A. Thaler, S. L. Bud'Ko, P. C. Canfield, A. Goldman, I. I. Mazin, and R. R. Prozorov, Uniaxial-strain mechanical detwinning of $CaFe_2As_2$ and $BaFe_2As_2$ crystals: Optical and transport study, Phys. Rev. B **81**, 184508 (2010).

[22] J.-H. Chu, J. G. Analytis, K. De Greve, P. L. McMahon, Z. Islam, Y. Yamamoto, and I. R. Fisher, In-plane resistivity anisotropy in an underdoped iron arsenide superconductor, Science **329**, 824 (2010).

[23] J. Giapintzakis, D. Ginsberg, and P.-D. Han, A method for obtaining single domain superconducting $YBa_2Cu_3O_{7-x}$ single crystals, J. Low Temp. Phys. **77**, 155 (1989).

[24] X. Y. Zheng, R. Feng, D. Ellis, and Y.-J. Kim, Bulk-sensitive imaging of twin domains in $La_{2-x}Sr_xCuO_4$ under uniaxial pressure, Appl. Phys. Lett. **113**, 071906 (2018).

[25] S. Lei, M. Gu, D. Puggioni, G. Stone, J. Peng, J. Ge, Y. Wang, B. Wang, Y. Yuan, K. Wang, Z. Mao, J. M. Rondinelli, and V.

Gopalan, Observation of quasi-two-dimensional polar domains and ferroelastic switching in a metal, $Ca_3Ru_2O_7$, Nano Lett. **18**, 3088 (2018).

[26] S. Mühlbauer, B. Binz, F. Jonietz, C. Pfleiderer, A. Rosch, A. Neubauer, R. Georgii, and P. Böni, Skyrmion lattice in a chiral magnet, Science **323**, 915 (2009).

[27] X. Yu, N. Kanazawa, Y. Onose, K. Kimoto, W. Zhang, S. Ishiwata, Y. Matsui, and Y. Tokura, Near room-temperature formation of a skyrmion crystal in thin-films of the helimagnet FeGe, Nat. Mater. **10**, 106 (2011).

[28] Y. Onose, Y. Okamura, S. Seki, S. Ishiwata, and Y. Tokura, Observation of Magnetic Excitations of Skyrmion Crystal in a Helimagnetic Insulator Cu_2OSeO_3, Phys. Rev. Lett. **109**, 037603 (2012).

[29] J. D. Bocarsly, R. F. Need, R. Seshadri, and S. D. Wilson, Magnetoentropic signatures of skyrmionic phase behavior in FeGe, Phys. Rev. B **97**, 100404(R) (2018).

[30] J. D. Bocarsly, C. Heikes, C. M. Brown, S. D. Wilson, and R. Seshadri, Deciphering structural and magnetic disorder in the chiral skyrmion host materials $Co_xZn_yMn_z(x+y+z=20)$, Phys. Rev. Mater. **3**, 014402 (2019).

[31] X. Zhang, Y. Zhou, K. M. Song, T.-E. Park, J. Xia, M. Ezawa, X. Liu, W. Zhao, G. Zhao, and S. Woo, Skyrmion-electronics: writing, deleting, reading and processing magnetic skyrmions toward spintronic applications, J. Phys.: Condens. Matter **32**, 143001 (2020).

[32] I. Dzyaloshinsky, A thermodynamic theory of "weak" ferromagnetism of antiferromagnetics, J. Phys. Chem. Solids **4**, 241 (1958).

[33] T. Moriya, Anisotropic superexchange interaction and weak ferromagnetism, Phys. Rev. **120**, 91 (1960).

[34] T. Okubo, S. Chung, and H. Kawamura, Multiple-q States and the Skyrmion Lattice of the Triangular-Lattice Heisenberg Antiferromagnet Under Magnetic Fields, Phys. Rev. Lett. **108**, 017206 (2012).

[35] A. Leonov and M. Mostovoy, Multiply periodic states and isolated skyrmions in an anisotropic frustrated magnet, Nat. Commun. **6**, 8275 (2015).

[36] S.-Z. Lin and S. Hayami, Ginzburg-Landau theory for skyrmions in inversion-symmetric magnets with competing interactions, Phys. Rev. B **93**, 064430 (2016).

[37] R. Ozawa, S. Hayami, and Y. Motome, Zero-Field Skyrmions with a High Topological Number in Itinerant Magnets, Phys. Rev. Lett. **118**, 147205 (2017).

[38] S. Hayami, R. Ozawa, and Y. Motome, Effective bilinear-biquadratic model for noncoplanar ordering in itinerant magnets, Phys. Rev. B **95**, 224424 (2017).

[39] T. Kurumaji, T. Nakajima, M. Hirschberger, A. Kikkawa, Y. Yamasaki, H. Sagayama, H. Nakao, Y. Taguchi, T.-h. Arima, and Y. Tokura, Skyrmion lattice with a giant topological hall effect in a frustrated triangular-lattice magnet, Science **365**, 914 (2019).

[40] M. Hirschberger, T. Nakajima, S. Gao, L. Peng, A. Kikkawa, T. Kurumaji, M. Kriener, Y. Yamasaki, H. Sagayama, H. Nakao *et al.*, Skyrmion phase and competing magnetic orders on a breathing kagomé lattice, Nat. Commun. **10**, 1 (2019).

[41] N. D. Khanh, T. Nakajima, X. Yu, S. Gao, K. Shibata, M. Hirschberger, Y. Yamasaki, H. Sagayama, H. Nakao, L. Peng *et al.*, Nanometric square skyrmion lattice in a centrosymmetric tetragonal magnet, Nat. Nanotechnol. **15**, 444 (2020).

[42] S. Nakamura, N. Kabeya, M. Kobayashi, K. Araki, K. Katoh, and A. Ochiai, Spin trimer formation in the metallic compound $Gd_3Ru_4Al_{12}$ with a distorted kagome lattice structure, Phys. Rev. B **98**, 054410 (2018).

[43] M. Ślaski, A. Szytuła, J. Leciejewicz, and A. Zygmunt, Magnetic properties of ReRu2Si2 (Re= Pr, Nd, Gd, Tb, Dy, Er) intermetallics, J. Magn. Magn. Mater. **46**, 114 (1984).

[44] A. Garnier, D. Gignoux, D. Schmitt, and T. Shigeoka, Giant magnetic anisotropy in tetragonal GdRu2Ge2 and GdRu2Si2, Phys. B: Condens. Matter **222**, 80 (1996).

[45] F. Tang, M. Frontzek, J. Dshemuchadse, T. Leisegang, M. Zschornak, R. Mietrach, J.-U. Hoffmann, W. Löser, S. Gemming, D. C. Meyer *et al.*, Crystallographic superstructure in R_2PdSi_3 compounds (R= heavy rare earth), Phys. Rev. B **84**, 104105 (2011).

[46] Y. Yasui, C. J. Butler, N. D. Khanh, S. Hayami, T. Nomoto, T. Hanaguri, Y. Motome, R. Arita, T.-h. Arima, Y. Tokura, and S. Seki. Imaging the coupling between itinerant electrons and localised moments in the centrosymmetric skyrmion magnet $GdRu_2Si_2$, Nat. Commun. **11**, 5925 (2020).

[47] Y. Tokunaga, X. Yu, J. White, H. M. Rønnow, D. Morikawa, Y. Taguchi, and Y. Tokura, A new class of chiral materials hosting magnetic skyrmions beyond room temperature, Nat. Commun. **6**, 7638 (2015).

[48] T. Kurumaji, T. Nakajima, V. Ukleev, A. Feoktystov, T.-h. Arima, K. Kakurai, and Y. Tokura, Néel-Type Skyrmion Lattice in the Tetragonal Polar Magnet $VOSe_2O_5$, Phys. Rev. Lett. **119**, 237201 (2017).

[49] X. Yu, Y. Onose, N. Kanazawa, J. Park, J. Han, Y. Matsui, N. Nagaosa, and Y. Tokura, Real-space observation of a two-dimensional skyrmion crystal, Nature **465**, 901 (2010).

[50] S. Seki, X. Yu, S. Ishiwata, and Y. Tokura, Observation of skyrmions in a multiferroic material, Science **336**, 198 (2012).

[51] I. Levatić, V. Šurija, H. Berger, and I. Živković, Dissipation processes in the insulating skyrmion compound Cu_2OSeO_3, Phys. Rev. B **90**, 224412 (2014).

[52] X. Zhang, Y. Zhou, and M. Ezawa, Antiferromagnetic skyrmion: Stability, creation and manipulation, Sci. Rep. **6**, 24795 (2016).

[53] J. Barker and O. A. Tretiakov, Static and Dynamical Properties of Antiferromagnetic Skyrmions in the Presence of Applied Current and Temperature, Phys. Rev. Lett. **116**, 147203 (2016).

[54] H. Velkov, O. Gomonay, M. Beens, G. Schwiete, A. Brataas, J. Sinova, and R. A. Duine, Phenomenology of current-induced skyrmion motion in antiferromagnets, New J. Phys. **18**, 075016 (2016).

[55] C. Jin, C. Song, J. Wang, and Q. Liu, Dynamics of antiferromagnetic skyrmion driven by the spin Hall effect, Appl. Phys. Lett. **109**, 182404 (2016).

[56] H. Fujita and M. Sato, Ultrafast generation of skyrmionic defects with vortex beams: Printing laser profiles on magnets, Phys. Rev. B **95**, 054421 (2017).

[57] B. Göbel, A. Mook, J. Henk, and I. Mertig, Antiferromagnetic skyrmion crystals: Generation, topological Hall, and topological spin Hall effect, Phys. Rev. B **96**, 060406(R) (2017).

[58] A. Salimath, F. Zhuo, R. Tomasello, G. Finocchio, and A. Manchon, Controlling the deformation of antiferromagnetic skyrmions in the high-velocity regime, Phys. Rev. B **101**, 024429 (2020).

[59] X. Zhang, Y. Zhou, and M. Ezawa, Magnetic bilayer-skyrmions without skyrmion Hall effect, Nat. Commun. **7**, 10293 (2016).

[60] N. Kolmakova, A. Sidorenko, and R. Levitin, Features of the magnetic properties of rare-earth intermetallides RMn_2Ge_2, Low Temp. Phys. **28**, 653 (2002).